Facilitation Induced Transparency and Single-Photon Switch with Dual-Channel Rydberg Interactions

Yao Ding[1], Zhengyang Bai[1],[*] Guoxiang Huang[1], and Weibin Li[2]

[1]*State Key Laboratory of Precision Spectroscopy, East China Normal University, Shanghai 200062, China*
[2]*School of Physics and Astronomy, and Centre for the Mathematics and Theoretical Physics of Quantum Non-equilibrium Systems,*
University of Nottingham, Nottingham, NG7 2RD, UK

(Dated: January 10, 2023)

We investigate facilitation induced transparency (FIT) enabled by strong and long-range Rydberg atom interactions between two spatially separated optical channels. In this setting, the resonant two-photon excitation of Rydberg states in a target channel is conditioned by a single Rydberg excitation in a control channel. Through the contactless coupling enabled by the Rydberg interaction, the optical transparency of the target channel can be actively manipulated by steering the optical detuning in the control channel. By adopting a dressed-state picture, we identify two different interference pathways, in which one corresponds to Rydberg blockade and an emergent one results from facilitation. We show that the FIT is originated from the Rydberg interaction and the quantum interference effect between the two pathways, which is different from conventional electromagnetically induced transparency realized by single-body laser-atom coupling. We find that the FIT in such a dual-channel setting is rather robust, insensitive to changes of systemic parameters, and can be generalized to multi-channel settings. Moreover, we demonstrate that such a FIT permits to realize controllable single-photon switches, which also paves a route to detect Rydberg facilitation by using optical absorption spectra. Our study contributes to current efforts in probing correlated many-body dynamics and developing single-photon quantum devices based on Rydberg atom ensembles.

I. INTRODUCTION

Cold gases of Rydberg atoms have emerged as a versatile platform for studying quantum nonlinear optics, non-equilibrium statistical physics, and quantum simulation of strongly interacting many-body systems [1–4], including antiferromagnetic phase transition [5, 6], quantum many-body scars [7–9], and Heisenberg XYZ spin model [10]. At the same time, Rydberg atoms are of technological importance, which allow to create collectively encoded qubit [11, 12], entanglement [13, 14], photonic or neutral-atom gates for quantum information processing [1, 15–17], precision measurements [18, 19], and so on. The enabled fundamental research and practical applications are rooted largely by the fact that Rydberg atoms offer strong and long-ranged interactions. In addition, their internal and external states can be actively manipulated under current experimental conditions [4, 20].

Rydberg many-body physics is largely based on two mechanisms: Rydberg blockade and facilitation (antiblockade), which can be realized by tuning the excitation laser on resonance with atomic transitions, and for matching the Rydberg interaction induced energy shifts [21], respectively. The former prevents multiple Rydberg excitations in the vicinity of a Rydberg atom, which benefits to the creation of quantum correlation and entanglement between atoms [13, 22]. The facilitation, opposite to the blockade, allows the formation of Rydberg clusters [15, 23–27]; it has been a central building block of non-equilibrium phase transitions, such as aggregation [25, 28], epidemic spreading [29, 30], and self-organized criticality [31, 32], etc.. Experimentally, Rydberg facilitation can be detected via absorption imaging [31] or direct ionization [33–35]. However, although these methods have high

efficiency, they typically damage many-body coherence after experimental operations [36].

In this work, we theoretically investigate the optical property of a dual-channel Rydberg ensemble [37–42], and illustrate that the facilitation mechanism can lead to an effective interaction to probe photons, which can be directly measured by using atomic absorption spectrum. The system we consider consists of two optical channels that are remotely separated in space, in which target channel A is resonantly excited to a Rydberg state via electromagnetically induced transparency (EIT) [43] and affected by control channel B via long-ranged Rydberg interactions. Such a setting is available to realize with present-day experimental techniques [39, 40, 42].

We show that a transparency window for probe photons opens through adjusting the detuning of the channel B, and this transparency window is sensitive to the Rydberg interaction. By using numerical and dressed-state calculations, we reveal many-body quantum pathways and characterize an interaction-dependent scaling function. A key finding is that the two resonant transition pathways are respectively originated from the Rydberg blockade and facilitation; it is the quantum interference effect between the two pathways that leads to the facilitation induced transparency (FIT) of the probe photons. The relevant model can moreover be generalized to Rydberg atomic gases with multiple optical channels.

The results on the FIT described above may have potential applications in all-optical quantum information processing. To realize optical quantum devices at single photon level, up to now various quantum systems have been suggested to implement optical switches or transistors, such as single molecules [44], quantum dots [45–48] and neutral atoms [49, 50]. However, due to the saturable absorption of single quantum emitters, it is difficult to realize a sizable optical non-linearity at single-photon level. To enhance light-matter interactions, one way is to use high-finesse optical res-

onators to confine photons to small mode volumes [51, 52]. At variance with single-body quantum systems, strong and long-range interactions between Rydberg atoms can be effectively mapped onto photon-photon interactions via two-photon scheme. This provides an alternative avenue to design single-photon switching in *free space* [53–55]. We demonstrate that the system proposed here can be used to design contactless single-photon switches, which is different from early studies, where Rydberg single-photon switches were realized in the blockade regime [42, 53–58]. By employing the presented dual-channel system, one can easily launch both facilitated and blockade single-photon switch by manipulating the control channel.

Moreover, different from that of stationary Rydberg single-photon switches reported before, the efficiency of the FIT-based photon switch suggested here can be controlled dynamically. The use of the dual-channel setting brings more potential benefits. Here Rydberg atoms in the control and target channels are spatially separated. For example, complicated atomic and molecular processes could be avoided, which play roles in the Rydberg blockade in atomic ensembles [59]. As we will show later, Rydberg populations in the FIT is relatively weak. This could mitigate the formation of ultralong-range Rydberg molecules [60, 61] and Rydberg polarons [62] due to collisions between ground state and Rydberg atoms [63]. These features mean that coherence of the atom could be increasingly protected in the FIT regime.

The remainder of the article is arranged as follows. In Sec. II, we introduce the Rydberg dual-channel model based on a master equation description. The level scheme and typically parameters are given. In Sec. III, we reveal the FIT mechanism through analyzing a two-atom model both analytically and numerically. In Sec. III A, coherence of the probe field is obtained numerically. By comparing with the approximate result, we reveal the importance of two-channel correlations in the emergence of FIT. In Sec. III B, we present an analytical dressed-state approach on the model and show the scaling of FIT as a function of the inter-channel interaction. In Sec. IV, based on the FIT we discuss controllable single-photon switch protocol. Finally, Sec. V gives a summary of the main results obtained in this work.

II. DUAL-CHANNEL RYDBERG MODEL

The system we consider consists of two ensembles of cold atoms driven by channel-dependent laser fields. The two ensembles are prepared in parallel, elongated traps along z direction, and separated by distance d; see Fig. 1(a). They form two optical channels, i.e. a target channel A (containing N_A atoms) and a control channel B (N_B atoms). The atomic level structure and the optical excitation scheme are illustrated schematically in Fig. 1(b). We assume that, in the target channel A, a weak probe laser field $\hat{\mathcal{E}}_p(z)$ [Rabi frequency $\hat{\Omega}_p(z) = g\hat{\mathcal{E}}_p(z)$] resonantly couples the ground state $|1\rangle$ and the excited state $|2\rangle$, and a coupling laser field (Rabi frequency Ω) resonantly couples the state $|2\rangle$ and the Rydberg state $|3\rangle$, which forms a scheme of conventional Rydberg-
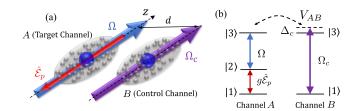

FIG. 1. **Scheme of dual-channel Rydberg atomic gas for realizing FIT.** Two atomic ensembles, i.e. target channel A and control channel B, are prepared in parallel and separated by distance d. (a) A weak probe field $\hat{\mathcal{E}}_p$ propagates in the channel A, whose dynamics is facilitated by the Rydberg excitation in the channel B. Long-range inter-channel Rydberg interaction permits a contactless control for the two channels and hence the propagation of the probe photon. (b) Level diagram and excitation scheme. Atoms in the channel A have three quantum states (i.e. $|1\rangle, |2\rangle, |3\rangle$; $|3\rangle$ is a Rydberg state) forming a Rydberg-EIT, where resonant transitions $|1\rangle \leftrightarrow |2\rangle$ and $|2\rangle \leftrightarrow |3\rangle$ are respectively provided by weak probe field $\hat{\mathcal{E}}_p$ and strong coupling field (Rabi frequency Ω). In the channel B, a control field with Rabi frequency Ω_c drives the transition between the ground state $|1\rangle$ to the Rydberg state $|3\rangle$ with detuning Δ_c. V_{AB} is the van der Waals interaction between the atoms in the two channels.

EIT [36]. Here $g = \mu_{21} \sqrt{\omega_p/(2\hbar\epsilon_0 V_p)}$ is the atom-field coupling constant, with ω_p the central angular frequency of the probe field, V_p the quantization volume of the probe field, and μ_{21} the electric-dipole matrix element associated with the transition between $|1\rangle$ and $|2\rangle$. In the control channel B, atomic levels $|1\rangle$ and $|3\rangle$ are coupled off-resonantly by another control laser field (Rabi frequency Ω_c) with detuning Δ_c, which plays a critical role for realizing the FIT. We assume that both Ω and Ω_c are strong enough, thus they can be taken as classical fields and their depletion are negligible.

Under the rotating wave approximation, by setting $\hbar = 1$ the Hamiltonian for the channels A and B are respectively given by

$$\hat{H}_A = -\frac{1}{2} \sum_{j \in A} \left[\hat{\Omega}_p \hat{\sigma}_{21}(z_j) + \Omega \hat{\sigma}_{32}(z_j) + \text{H.c.} \right], \quad \text{(1a)}$$

$$\hat{H}_B = -\sum_{j \in B} \left[\frac{\Omega_c}{2} \hat{\sigma}_{31}(z_j) - \Delta_c \hat{\sigma}_{33}(z_j) + \text{H.c.} \right], \quad \text{(1b)}$$

with $\hat{\sigma}_{ab}(z_j) \equiv |a_j\rangle\langle b_j|$ (z_j is the position of jth atom in the respective ensemble) and H.c. representing Hermitian conjugate of the preceding terms. We assume that the spatial extension of each atomic ensemble is small, so that multiple Rydberg excitations within each ensemble is prohibited by the strong and long-ranged interaction between Rydberg states. However, there exists an inter-channel Rydberg interaction between the target channel A and the control channel B (with the distance d typically Rydberg blockade radius $\sim 5-10\,\mu\text{m}$), which leads to the following inter-channel interaction Hamiltonian

$$H_{\text{int}} = \sum_{j \in A, l \in B} V(z_{jl}) \hat{\sigma}_{33}(z_j) \hat{\sigma}_{33}(z_l), \quad \text{(2)}$$

Here we have assumed that the target and control channels are both excited to $|nS\rangle$ states (or $|nD\rangle$ states). Two Rydberg channels interact via the van der Waals (vdW) interaction $V(z_{jl}) = -C_6/[(z_j - z_l)^2 + d^2]^3$, with C_6 the dispersion coefficient. Note that, except for the vdW interaction, a

resonant dipole-dipole interaction can also be engineered by coupling the ensembles to Rydberg states $|S\rangle$ and $|P\rangle$, which may lead to spin-exchange between remote Rydberg channels [22, 38, 40, 41]. This is a topic deserving to be explored, but here we focus our consideration only on the case of the vdW interaction.

The dynamics of the system including the two channels is governed by the master equation,

$$\frac{d\rho}{dt} = -i\,[H,\rho] + D(\rho) + D_d(\rho), \qquad (3)$$

where $\rho(t)$ is density matrix, and $\hat{H} = \hat{H}_A + \hat{H}_B + H_{\text{int}}$ is the total Hamiltonian of the system. In Eq. (3)

$$D(\rho) = \sum_{\mu=A,B} \sum_{j\in\mu} \Gamma_{ba}^{\mu} \Big\{ \hat{\sigma}_{ba}(z_j)\rho\hat{\sigma}_{ab}(z_j)$$
$$- \frac{1}{2}\Big[\rho\hat{\sigma}_{ab}(z_j)\hat{\sigma}_{ba}(z_j) + \hat{\sigma}_{ab}(z_j)\hat{\sigma}_{ba}(z_j)\rho\Big]\Big\}, \quad (4)$$

describes the respective dissipation processes from $|a\rangle \to |b\rangle$ with the rates $\Gamma_{ba}^{\mu} = \Gamma_{12}^{A}$, Γ_{23}^{A}, and Γ_{13}^{B};

$$D_d(\rho) = \sum_{\mu=A,B} \sum_{j\in\mu} \gamma_a^{\mu} \Big\{ 2\hat{\sigma}_{aa}(z_j)\rho\hat{\sigma}_{aa}(z_j) - \big[\rho\hat{\sigma}_{aa}(z_j) + \hat{\sigma}_{aa}(z_j)\rho\big]\Big\},$$
$$(5)$$

gives the dephasing of the atomic coherence (originated from atomic collisions, residue Doppler effect, dipole-dipole interaction between the Rydberg atoms, finite laser linewidth, etc.), with rates γ_a^{μ} ($\mu = A, B$; $a = 2, 3$). In the following, for the convenience of numerical calculations, we measure all atomic parameters (e.g. Ω_c, Ω_p, Δ_c) in unit of Γ_{12}^{A} (typically, $\Gamma_{12}^{A} \simeq 2\pi \times 6.06\,\text{MHz}$ for $|5P_{3/2}\rangle$ state in Rb atom; $\Gamma_{12}^{A} \simeq 2\pi \times 5.22\,\text{MHz}$ for $|6P_{3/2}\rangle$ state in Cs atom [64]).

In this setting, the inter-channel interaction is the central element in the Hamiltonian, with which the dynamics of the target channel A can be actively manipulated by varying the relevant atomic parameters in the control channel B (i.e., Ω_c, Δ_c). Note that the control channel B is adopted with a two-photon Raman scheme. Due to the large single-photon detuning, the channel B can be described by an effective two-level system. Though this is a simplified approach, it can demonstrate the essential physics inherent in the model. Dynamics of the two-photon scheme in channel B is presented in Appendix A and will be briefly discussed below in Fig. 3(c).

III. FACILITATION INDUCED TRANSPARENCY

In order to demonstrate the FIT and to reveal its basic physical mechanism, we first consider a simple two-atom scenario [i.e. one atom (atom A) is in the channel A and another one (the atom B) is in the channel B] that represents the minimal model of the dual-channel setting [22, 38].

With such a consideration, the effective Hamiltonian is reduced into the form of $\hat{H} = \hat{H}_A + \hat{H}_B + \hat{H}_{\text{int}}$, where $\hat{H}_A = -(\hat{\Omega}_p\hat{\sigma}_{21}^{A}/2 + \Omega\hat{\sigma}_{32}^{A}/2) + \text{H.c.}$, $\hat{H}_B = -\Omega_c\hat{\sigma}_{31}^{B}/2 + \Delta_c\hat{\sigma}_{33}^{B} + \text{H.c.}$, and $H_{\text{int}} = V_{AB}\hat{\sigma}_{33}^{A}\hat{\sigma}_{33}^{B}$. Here $\hat{\sigma}_{ab}^{A} = \hat{\sigma}_{ab}(z_A)$, $\hat{\sigma}_{ab}^{B} = \hat{\sigma}_{ab}(z_B)$,

the two-body interaction is given by $V_{AB} = -C_6/d^6$. Note that under the EIT condition the probe field has negligible attenuation and can be approximately treated as a classical one [65], hence for simplicity we replace $\hat{\Omega}_p$ by Ω_p in the approach of this section. The spatial-temporal dynamics of the quantized probe field at a level of single photon [56, 66, 67] in high density atom gases will be analyzed in section IV.

A. Optical coherence and inter-channel correlation

The response character of the system to the probe field is characterized by the atomic coherence between the states $|1\rangle$ and $|2\rangle$ in the channel A, i.e. ρ_{21}^{A}, where $\rho_{ab}^{\mu} \equiv \text{Tr}(\rho\sigma_{ba}^{\mu})$ ($\mu = A, B$) are one-body reduced density matrix (DM) elements. The absorption (refraction) of the probe field is determined by the imaginary (real) part $\text{Im}(\rho_{21}^{A})$ [$\text{Re}(\rho_{21}^{A})$] of ρ_{21}^{A}. The corresponding optical susceptibility will be given in section IV; see Eq. (14) below. In the following calculations, we shall examine in particular the behavior of ρ_{21}^{A} when adjusting the detuning Δ_c in the channel B, which is one of the system parameters easy to control experimentally.
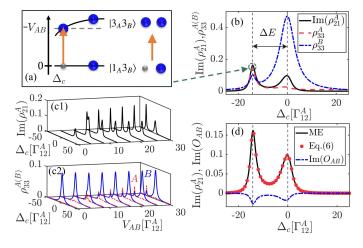

FIG. 2. **Optical coherence and inter-channel correlation in the two-atom system.** (a) Level diagram and excitation scheme between the Rydberg blockade state $|1_A 3_B\rangle$ (occurring at $\Delta_c = 0$) to the facilitated state $|3_A 3_B\rangle$ (occurring at $\Delta_c = -V_{AB}$) of the two-atom system. For more details, see the text. (b) FIT transparency window induced by the inter-channel interaction V_{AB}, as seen in the absorption spectrum $\text{Im}(\rho_{21}^{A})$ as a function of Δ_c. ΔE is the energy separation between centers of the two peaks of the FIT spectrum. (c1) $\text{Im}(\rho_{21}^{A})$ as a function of Δ_c and V_{AB}. $\text{Im}(\rho_{21}^{A})$ exhibits a single peak for smaller V_{AB}; it however splits into two peaks for larger V_{AB}. The dip between the two peaks becomes wider and deeper as V_{AB} increases, similar to the behavior of EIT in three-level systems. Corresponding Rydberg excitations are shown in (b) (dashed red line for ρ_{33}^{A}; dot-dashed blue line for ρ_{33}^{B}), and also in (c2) which shows that the channel A is fully blockaded independent of V_{AB} (solid blue line) for $\Delta_c = 0$ but ρ_{33}^{A} is facilitated around $\Delta_c = -V_{AB}$ (dashed red line). (d) Analytical result (dotted red line) given by Eq. (6), which captures well with the one by solving the master equation (ME) numerically (solid black line). The quantum correlation O_{AB} (dot-dashed blue line) is significant for the FIT effect. The parameters used are $\Omega = \Omega_c = 5\Gamma_{12}^{A}$, $\Omega_p = 0.5\Gamma_{12}^{A}$, $\Gamma_{23}^{A} = 10^{-3}\Gamma_{12}^{A}$, and $\Gamma_{13}^{B} = \Gamma_{12}^{A}$; in panels (b) and (d), $V_{AB} = 15\Gamma_{12}^{A}$.

Fig. 2(b) shows the result on the absorption spectrum

Im(ρ_{21}^A) as a function of Δ_c through solving the master equation (3) numerically. We see that Im(ρ_{21}^A) has an EIT-like pattern, where a transparent window (called *FIT transparent window* hereafter) in the absorption spectrum opens. For weak inter-channel interaction (i.e. small V_{AB}), Im(ρ_{21}^A) displays only a single absorption peak, while for stronger interaction (i.e. larger V_{AB}) two absorption peaks occur [see Fig. 2(c1)]. Concretely, in the region of large V_{AB}, one peak (the lower one) locates at $\Delta_c = 0$ and the other (the higher one) locates at $\Delta_c = -V_{AB}$. The width of the two peaks is ΔE [see Fig. 2(b)]. Our calculating result also shows that ρ_{21}^A strongly correlates to Rydberg populations ρ_{33}^A and ρ_{33}^B.

In Fig. 2(c1), one can observe clearly that there is a crossover from one peak to two ones for Im(ρ_{21}^A) through the adjustment of V_{AB}, and the transparent window becomes wider and deeper as inter-channel interaction V_{AB} increases. This fact tells us that the splitting of the probe-field absorption spectrum (i.e. FIT) is facilitated by the contribution of the inter-channel interaction V_{AB}. For illustrating this point further, the left part of Fig. 2(a) [which corresponds to the point indicated by the small green circle in Fig. 2(b)] gives the level diagram and excitation scheme between the Ryder blockade state $|1_A3_B\rangle$ (occurring for $\Delta_c = 0$) to the facilitated state $|3_A3_B\rangle$ (occurring for $\Delta_c = -V_{AB}$) of the two-atom model; the solid gray circles (solid blue circles) denote ground-state (Rydberg state) atoms. The right part of the figure is a simplified representation of the excitation scheme showing in the left part. Although the transition of the target atom A to the Rydberg state acquires an energy shift because of the inter-channel interaction V_{AB}, by sweeping the detuning Δ_c in the channel B the system can be driven from the Rydberg blockade state $|1_A3_B\rangle$ to the facilitated state $|3_A3_B\rangle$, where the channels A and B are simultaneously excited to the Rydberg state near at $\Delta_c = -V_{AB}$ [see Fig. 2(b) and (c2)]. Since the positions of the excitation blockade and the facilitation overlaps well with the peaks of Im(ρ_{21}^A), the FIT transparency window between the two strong absorption peaks is thus induced by the both effects of the excitation blockade and the facilitation.

To verify the behavior of the atomic coherence and the FIT phenomenon in a direct way, we have solved the Heisenberg equations of motion of the system. The calculation shows that ρ_{21}^A is given by the following form

$$\rho_{21}^A \simeq -\frac{2V_{AB}\rho_{31,33}^{AB}}{\Omega}, \tag{6}$$

where $\rho_{31,33}^{AB} \equiv \langle \hat{\sigma}_{13}^A \hat{\sigma}_{33}^B \rangle$ is two-body DM element (two-body correlator) [see Appendix B for details].

The result predicted by using this approach is plotted in Fig. 2(d) by a dotted red line. One sees that the analytical (6) captures well with the one by solving the master equation (ME) numerically (given by the solid black line). One notes that the variance $O_{AB} = \langle \hat{\sigma}_{13}^A \hat{\sigma}_{33}^B \rangle - \langle \hat{\sigma}_{13}^A \rangle \langle \hat{\sigma}_{33}^B \rangle = \rho_{31,33}^{AB} - \rho_{31}^A \rho_{33}^B$ exhibits the similar double peak structure of the FIT. In the above calculations, system parameters used are $\Omega = \Omega_c = 5\Gamma_{12}^A$, $\Omega_p = 0.5\Gamma_{12}^A$, $\Gamma_{23}^A = 10^{-3}\Gamma_{12}^A$, $\Gamma_{13}^B = \Gamma_{12}^A$, and $V_{AB} = 15\Gamma_{12}^A$ in panels (b) and (d). Based on the results described in Fig. 2, we conclude that FIT is mainly contributed by the inter-channel quantum correlation, contributed by the

Rydberg interaction between the atom A and the atom B. It should be stressed that such results cannot be predicted by using the approach of mean field theory [43, 68]. This indicates that the two-body correlation could be effectively mapped to the atomic coherence ρ_{21}^A, providing a method to detect Rydberg facilitation directly from the optical absorption spectrum, which is the key finding of this work.

B. Excitation pathways identified through dressed-state approach and generation to multiple target channels

Even when the system involves only two atoms, it is difficult to solve the master equation analytically (e.g. 36 coupled differential equations are involved). Motivated by the dressed-state theory of conventional EIT [69], here we develop an analytical approach of dressed state to identify the excitation pathways of the FIT through the facilitated many-body states.

We consider the interaction-dressed subspace spanned by the tensor product of two single-atom basis, i.e. $\{|2_A\rangle, |3_A\rangle\} \otimes \{|1_B\rangle, |3_B\rangle\}$, indicated by the dashed gray box in Fig. 3(a). The subspace is coupled by the ground state $|1_A\rangle$ of the channel A through the probe field Ω_p. For simplicity and for obtaining explicit analytical results, we neglect the small damping (i.e. the spontaneous emission and dephasing). The eigenspectra ϵ_j of the subspace can be obtained via the diagonalization of the system Hamiltonian (see Appendix C) expanded in this subspace, with corresponding set of eigen basis given by $\{|\psi_j\rangle; j = 1, 2, 3, 4\}$.

To highlight the roles played by the control channel B, we make a calculation especially on the eigenspectra and eigenfunctions. Shown in Fig. 3(b) is the result for the eigenvalues ϵ_j as functions of Δ_c for $V_{AB} = 15\Gamma_{12}^A$. Corresponding eigenstates $\{|\psi_j\rangle; j = 1, 4\}$ and $\{|\psi_j\rangle; j = 2, 3\}$ are given by the dashed gray and solid blue lines, respectively. We see that the prove field Ω_p can resonantly drive the transition $|1_A\rangle \rightarrow |\Psi_F\rangle$ ($|1_A\rangle \rightarrow |\Psi_E\rangle$) at $\Delta_c = \Delta_c^-$ ($\Delta_c = \Delta_c^+$), where $|\Psi_E\rangle$ ($|\Psi_F\rangle$) is the blockade (facilitation) state. For more details, see the discussion given in the Appendix C.

From the figure, we see that, when $\epsilon_j = 0$, the probe field Ω_p can resonantly drive the transition from $|1_A\rangle$ to the dressed subspace at the particular detuning $\Delta_c^\pm = -V_{AB}/2 \pm \sqrt{V_{AB}^2 + (\Omega - \Omega_c^2/\Omega)^2}/2$, which locates the double peaks of the absorption spectrum Im(ρ_{21}^A) [predicted also in Fig. 2(b)], with energy separation $\Delta E = \Delta_c^+ - \Delta_c^-$. In the strong interaction dominant regime (i.e. $|V_{AB}| > |\Omega|$, $|\Omega_c| \gg |\Omega - \Omega_c^2/\Omega|$), one can obtain $\Delta E \simeq V_{AB}$. This linear dependence on V_{AB} for the distance between the two absorption peaks can also be seen in the numerical data given by Fig. 3(c). Deviations for smaller V_{AB} attribute to spontaneous emission, dephasing of the atomic coherence and light induced shifts, which are included in the numerical simulation. In Fig. 3(c), the result for the case when the control channel described by three-level (3L) model (e.g. two-photon Raman scheme) is also shown. One sees that the energy separation ΔE as a function V_{AB} also have a linear dependence for large V_{AB}.

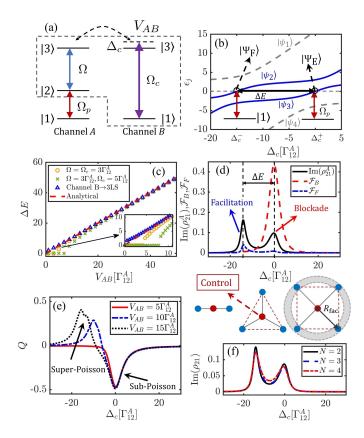Now lets turn to investigating the eigenstates of the system,

FIG. 3. **Dressed-state picture and the scaling of the FIT peak.** (a) Interaction-dressed subspace spanned by the basis $\{|2_A\rangle, |3_A\rangle\} \otimes \{|1_B\rangle, |3_B\rangle\}$, indicated by the dashed gray box. (b) Dressed eigen values ϵ_j as functions of Δ_c for $V_{AB} = 15\Gamma_{12}^A$; corresponding eigenstates $\{|\psi_j\rangle; j = 1, 4\}$ (dashed gray lines) and $\{|\psi_j\rangle; j = 2, 3\}$ (solid blue lines) are also shown. Ω_p can resonantly drive the transition $|1_A\rangle \rightarrow |\Psi_F\rangle$ ($|1_A\rangle \rightarrow |\Psi_E\rangle$) at $\Delta_c = \Delta_c^-$ ($\Delta_c = \Delta_c^+$), where $|\Psi_E\rangle$ ($|\Psi_F\rangle$) is the blockade (facilitation) state (see the Appendix C). (c) Energy separation ΔE [described also in Fig. 2(a)] as a function V_{AB} for $\Omega_c = 3\Gamma_{12}^A$ (yellow circles) and $\Omega_c = 5\Gamma_{12}^A$ (green crosses) with fixed $\Omega = 3\Gamma_{12}^A$ and $\Gamma_{13}^B = 0.1\Gamma_{12}^A$, obtained by numerically solving the master equation (3). Triangles: the result for the channel B is driven by a three level scheme (3LS). Inset: details of ΔE in the different parameter regimes for small V_{AB}. Dashed red line: the line $\Delta E = V_{AB}$, which matches well with the numerical data for larger V_{AB}. (d) Fidelities $\mathcal{F}_B$ (dashed red line) and $\mathcal{F}_F$ (dash-dotted blue line) as functions of Δ_c. Maximal fidelities overlap with the doublet peaks of the absorption spectrum $\text{Im}(\rho_{21}^A)$ (solid black line). (e) Mandel Q factor as a function of Δ_c for different V_{AB}, which is enhanced drastically at $\Delta_c = \Delta_c^\pm$ for large V_{AB}. (f) Suggested model with multiple target channels, in which the control channel (solid red circle) locates at the center of a ring (with radius R_{fac}) where the target channels (solid blue circles) locate. Such a setting can facilitates the excitation of N-target channels (solid blue circles) within a shell (gray region). Shown in the box are lines of $\text{Im}(\rho_{21})$ for $N = 2, 3, 4$, indicating that FIT is supported for such a system.

which, in the interaction dominant region, are given by

$$|\Psi_E\rangle = \frac{1}{\sqrt{2}}(|3_A 1_B\rangle - |2_A 3_B\rangle), \quad \text{for } \Delta_c = \Delta_c^+, \qquad (7)$$

$$|\Psi_F\rangle = \frac{1}{\sqrt{2}}(|3_A 3_B\rangle - |2_A 1_B\rangle), \quad \text{for } \Delta_c = \Delta_c^-, \qquad (8)$$

where $|\Psi_{E(F)}\rangle$ are Rydberg entangled and facilitated Bell states. The excitation of these states provides two pathways. When the inter-channel interaction is strong, they interfere

destructively and lead to the FIT. However, due to the weak probe field and the large spontaneous emission at the intermediate level $|2_A\rangle$, the entangled state $|\Psi_E\rangle$ decays to the blockade state $|\Psi_B\rangle = |1_A 3_B\rangle$, which partially destroys the transparency between the two absorption peaks, consisted with the result given in Fig. 2.

To verify the validity of the dressed-state approach in the presence of dissipation, we quantify the difference between states $\hat{\rho}_{B(F)} = |\Psi_{B(F)}\rangle\langle\Psi_{B(F)}|$ and the steady state $\hat{\rho}_s$ from master equation simulations with fidelity $\mathcal{F}_{B(F)} = (\text{Tr}|\sqrt{\hat{\rho}_{B(F)}}\sqrt{\hat{\rho}_s}|)^2$. When sweeping Δ_c, $\mathcal{F}_{B(F)}$ indeed displays maxima at $\Delta_c^\pm$ [see Fig. 3(d)]. This indicates that the dressed-states can be used to characterize the Rydberg blockade and facilitation in the mixed-state system.

We emphasize that two-body quantum correlations are important to the FIT. We further quantify the inter-channel correlation by the Mandel Q factor defined as $Q = \langle(\Delta\hat{n}_{33})^2\rangle/\langle\hat{n}_{33}\rangle - 1$ with $\hat{n}_{33} = \hat{\sigma}_{33}^A + \hat{\sigma}_{33}^B$. As illustrated in Fig. 3(e), Mandel Q factor is enhanced drastically at $\Delta_c = \Delta_c^\pm$, and exhibits sub-Poissonian counting statistics with $Q < 0$ around $\Delta_c = \Delta_c^+$, and the super-Poissonian processes characterized by $Q > 0$ around $\Delta_c = \Delta_c^-$. This is an unique property for such a system, where exotic statistics characteristics can be probed via tuning laser parameters [25, 70].

The dual channel model discussed above can be extended to the situations with multiple target channels. One possible generation is sketched in Fig. 3(f), in which the control channel (denoted by the solid red circle) locates at the center of a ring (with radius R_{fac}) where the target channels (denoted by solid blue circles) locate. Such a setting can facilitates the excitation of N-target channels (represented by solid blue circles) within a shell (represented by the gray region) [28]. The lower part of the figure (i.e. the box) shows the lines of the probe-field absorption spectrum $\text{Im}(\rho_{21})$ for the target-channel number $N = 2, 3, 4$, which indicates that FIT character still persists with multiple target channels.

In our simulation, interactions between different target channels have been taken into account. Due to the strong interaction contributed from the control channel, the target channels are fully blockade or facilitated, and thus the target-target (TT) interaction plays a minor role on the FIT [26, 31]. To demonstrate this point further, we have constructed a three-atom FIT model (in which one control atom and two target atoms are considered) and investigated its FIT behavior. The results shows that the TT interaction have a small effect on the FIT in the system; for more detail, see Appendix D.

IV. FACILITATED SINGLE-PHOTON SWITCH PROTOCOL

The above analysis shows that the target channel A can be changed from opaque to transparent by tuning Δ_c. Such tunability allows us to design optical switch via FIT by using contactless atom-atom interactions. In the rest of the work, we consider the propagation dynamics of quantized probe fields in high density atom gases. We will show that a facilitated single-photon switch can be realized in the dual-channel sys-

tem suggested above.

A. Optical susceptibility of the probe field

Before examining quantum dynamics of the single-photon switch, we first analyze the polarization of the probe field $\mathcal{E}_p$, defined by $P_p \equiv \epsilon_0 \chi_p \mathcal{E}_p$. The susceptibility χ_p is, in general, of a nonlinear function of $\mathcal{E}_p$ if the probe-field intensity is high. The relation between the optical susceptibility of the probe field and the one-body DM elements can be built with the formula

$$\chi_p = \frac{\hbar \varepsilon_0}{\mathcal{N}_A \mu_{21}^2 \Omega_p} \rho_{21}^A, \tag{9}$$

where $\mathcal{N}_A$ is the atomic density of the ensemble A (assumed to be homogeneous). In our setting, χ_p depends not only on the parameters of the ensemble A (e.g, Ω_p, Ω), but also on those of the ensemble B (e.g., Ω_c, Δ_c).
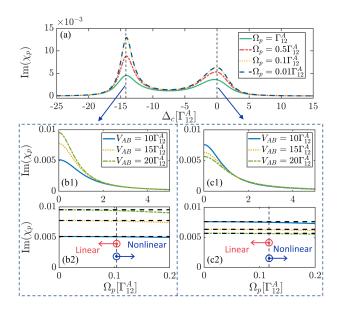

FIG. 4. **Optical susceptibility.** (a) $\text{Im}(\chi_p)$ as a function of Δ_c (for $V_{AB} = 15\Gamma_{12}^A$) when the Rabi frequency of the probe field takes values of $0.01\Gamma_{12}^A, 0.1\Gamma_{12}^A, 0.5\Gamma_{12}^A,$ and Γ_{12}^A, respectively. (b1) $\text{Im}(\chi_p)$ as a function of Ω_p and V_{AB} for $\Delta_c = -V_{AB}$ [corresponding to the left peak of panel (a)]. (b2) The same as (b1) but for small values of Ω_p. (c1) and (c2): The same as (b1) and (b2) but with $\Delta_c = 0$ [corresponding to the right peak of panel (a)]. The result shows that when decreasing Ω_p, $\text{Im}(\chi_p)$ saturates for $\Omega_p < 0.1\Gamma_{12}^A$, such that χ_p behaves as a linear susceptibility, independent of Ω_p.

Figure 4(a) shows the imaginary part of the susceptibility $\text{Im}(\chi_p)$ as a function of Rabi frequency of the probe field, Ω_p, with fixed $V_{AB} = 15\Gamma_{12}^A$. The dashed blue, dotted yellow, dot-dashed red, and solid green lines are for $\Omega_p = 0.01\Gamma_{12}^A, 0.1\Gamma_{12}^A, 0.5\Gamma_{12}^A,$ and Γ_{12}^A, respectively. Illustrated in panels (b1) is $\text{Im}(\chi_p)$ as a function of Ω_p and V_{AB} for $\Delta_c = -V_{AB}$, which corresponds to the left peak of panel (a); panel (b2) is same as panel (b1) but for small values of Ω_p. Panels (c1) and (c2) are the same as (b1) and (b2) but with $\Delta_c = 0$ [corresponding to the right peak of panel

(a)]. The results are obtained by solving the Heisenberg equations of the system. From the figure we see that, as the probe Rabi frequency is decreased, there is a dramatic enhancement of $\text{Im}(\chi_p)$ around $\Delta_c = 0$ and $-V_{AB}$, manifested by the two FIT peaks in the figure. Moreover, there is no broadening or detuning of the FIT, and the susceptibility saturates when $\Omega_p < 0.1\Gamma_{12}^A$, for which $\text{Im}(\chi_p)$ does not change as Ω_p is decreased. The absence of the broadening or shift is vital for the detection of Rydberg facilitation from the optical absorption spectrum. When the probe field is weak (e.g. at the level of single photons), χ_p becomes linear, i.e. its value is largely independent of $\mathcal{E}_p$ in both the facilitation and blockade region [see Fig. 4(b2) and (c2)]. Outside the linear regime, one can achieve a strong Rydberg nonlinearity in such a system, which is a topic deserving explorations but beyond the scope of the present work.

B. Facilitated single-photon switch

In the following, we will focus on the linear regime and demonstrate how to realize a single-photon switch with the FIT predicted above. To this end, we consider an elongated atomic gas and study propagation of the probe field along the z direction, while neglecting diffraction effect, which is valid for the case of short propagation distance or the atomic gas is prepared in a trap with a small transverse cross section [39, 42, 54]. Treating the probe field quantum mechanically, the dynamics of its propagation is governed by the Hamiltonian $\hat{H}_p = -(c/L) \int dz \hat{\mathcal{E}}_p^\dagger(z,t) i \partial_z \hat{\mathcal{E}}_p(z,t)$. Here, $\hat{\mathcal{E}}_p(z,t)$ is the slowly varying annihilation operator of probe photons, satisfying the equal-time commutation relation $[\hat{\mathcal{E}}_p(z,t), \hat{\mathcal{E}}_p^\dagger(z',t)] = L\delta(z - z')$, with L the quantization length along the z axis. By applying the continuous density approximation [66] the Hamiltonian of the system reads

$$\hat{H}_A = -\frac{N_A}{L} \int dz \left[\frac{g\hat{\mathcal{E}}_p(z,t)}{2} \hat{\sigma}_{21}^A(z,t) + \frac{\Omega}{2} \hat{\sigma}_{32}^A(z,t) + \text{H.c.} \right], \tag{10a}$$

$$\hat{H}_B = -\frac{N_B}{L} \int dz \left[\frac{\Omega_c}{2} \hat{\sigma}_{31}^B(z,t) - \Delta_c \hat{\sigma}_{33}^B(z,t) + \text{H.c.} \right], \tag{10b}$$

here N_A and N_A are respectively atomic numbers in the channels A and B, $\hat{\sigma}_{ab}^\mu(z)$ satisfies the canonical commutation relation $[\hat{\sigma}_{ab}^\mu(z), \hat{\sigma}_{cd}^\mu(z')] = \delta(z - z')[\delta_{bc}\hat{\sigma}_{ad}^\mu(z) - \delta_{da}\hat{\sigma}_{cb}^\mu(z)]L/N_\mu$. The Hamiltonian describing the inter-channel interaction is given by

$$H_{\text{int}} = \frac{N_A}{L} \sum_j \int dz V(z - z_j) \hat{\sigma}_{33}^A(z,t) \hat{\sigma}_{33}^B(z_j,t), \tag{11}$$

where the index j labels the respective Rydberg excitation in the channel B [56]. We assume that the atoms within each channel are trapped within a small spatial interval $\delta r \ll d$; the atom-atom interaction is described by the potential $V(z - z_j) \simeq -C_6/[(z - z_j)^2 + d^2]^3$ with $V_{AB} = -C_6/d^6$ [39].

Suppose that the quantum state of the single-photon input probe field has the form $|\Psi_P\rangle = (1/L) \int dz E_p(z,t) \hat{\mathcal{E}}_p^\dagger(z,t)|0\rangle$,

where $E_p(z,t)$ is the single-photon probability amplitude. Based on the Maxwell equation for $\hat{\mathcal{E}}_p(z,t)$, one can derive the evolution equation for $E_p(z,t)$ [65, 71], which reads

$$\left(\frac{\partial}{\partial t} + c\frac{\partial}{\partial z}\right)E_p(z,t) = ig\,N_A\rho_{21}^A(z,t)/2. \qquad (12)$$

It can be solved numerically in conjunction with the Bloch equations for the atomic DM elements ρ_{ab}^A and ρ_{ab}^B. The transmission T of the single-photon probe field, used to quantify efficiency of the photon switch, can be obtained at $z = L$, i.e. $T = \mathcal{I}_s(L)$, where $\mathcal{I}_s(z) = |E_p(z)|^2/|E_p(0)|^2$ is the relative intensity of the photon field at position z.

To understand the propagation dynamics of the probe photon, lets first consider a simple scenario in which the Rydberg excitation in the control channel B is localized at $z = 0$. Far-away from $z = 0$, the photon field can propagate under perfectly EIT condition in the channel A [where the excitation scheme is the one of an exact ladder-type EIT; see Fig. 1(a)], as illustrated in Fig. 5(a1). However, in close proximity to

FIG. 5. **Facilitation enabled single-photon switch.** (a) The control channel B is driven with the excitation localized at $z = 0$ (a1). In the vicinity of $z = 0$, ρ_{33}^A is blockaded for $\Delta_c = 0$ or facilitated for $\Delta_c = -V_{AB}$ ($\Delta_c = -V_{AB}/2$ is an intermediate case). They both result in a strong photon scattering, as can be seen from the decreasing relative intensity $\mathcal{I}_s$ (a2). Shown in (a3) and (a4) are ρ_{33}^A and ρ_{33}^B as functions of z for $\Delta_c = 0$ (red dashed line), $-V_{AB}/2$ (green dash-dotted line), and $-V_{AB}$ (blue solid line), respectively. (b) When the channel B is dynamically driven (b1), one can change the control detuning Δ_c from a far-detuned value to $-V_{AB}$ (or 0) to launch facilitated (blockade) single-photon switch, where the relative intensity of the probe field quickly decreases to zero (b2). Shown in (b3) and (b4) are ρ_{33}^A and ρ_{33}^B as functions of z for $\Delta_{cF} = 0$ (red dashed line), and $-V_{AB}$ (blue solid line), respectively. In the simulation, system parameters $\Omega = \Omega_c = 3\Gamma_{12}^A$, $V_{AB} = 15\Gamma_{12}^A$, and $\mathcal{N}_A = 3 \times 10^{12}\text{cm}^{-3}$ are used. See text for more details.

$z = 0$ (noticing that V_{AB} varies with z and reaches its maximal value V_{AB} at $z = 0$), the channel B inhibits ($\Delta_c = 0$) or

facilitates ($\Delta_c = -V_{AB}$) the Rydberg excitation in the channel A, and causes strong photon loss from the medium; see Fig. 5(a2), where $\mathcal{I}_s$ as a function of z is plotted for $\Delta_c = 0$, $\Delta_c = -V_{AB}/2$, and $\Delta_c = -V_{AB}$, respectively. The former (i.e. the result for $\Delta_c = 0$) is the phenomenon of Rydberg blockade, which has been studied in Ref. [53, 54, 56]; the latter (i.e. the result for $\Delta_c = -V_{AB}$) behaves as a *facilitated photon switch* where the probability of the Rydberg excitation in the both channels is relatively large. This can be seen clearly in Fig. 5(a3) and (a4), where ρ_{33}^A and ρ_{33}^B as functions of z. When passing from the interaction region, the photon field propagates freely again under the EIT condition where the photon scattering is negligible. Therefore, the reduced transmission is caused by the facilitation induced photon scattering in the vicinity of $z = 0$.
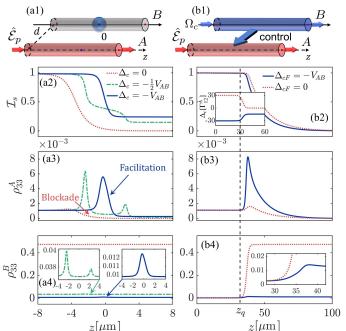
For an ideal photon switch, the photon field should be completely blocked from transmission (i.e. $T = 0$). To achieve this, we consider the light field in the control channel co-propagate with the probe field in the target channel, depicted in Fig. 5(b1). To demonstrate the controllability of the photon switch, the detuning Δ_c is chosen to be time-dependent but varies slowly, which has the from of $\Delta_c = \Delta_{c0} + (\Delta_{c0} - \Delta_{cF})[\tanh(1 - (z - z_q)/z_s) - 1]/2$ [see the inset of Fig. 5(b2)]. Initially, Ω_c is far detuned before the photon field travels to $z = z_q$. Then it is rapidly changed to $\Delta_{cF} \simeq -V_{AB}$ (or 0). In response to such changes, the system immediately evolves from a non-interacting dark states into an absorbing facilitated state (or blockade state) [see the behavior of $\rho_{33}^{A(B)}$ shown in Fig. 5(b3)-(b4)]. The transmission of the photon field quickly decreases from almost 100% to zero within a short propagation distance. Consequently, for a medium of less than 100 μm, the photon field transmission can be made completely vanish, which is promising for designing highly efficient and controllable single-photon switches.

C. Discussion on delocalized control-atom excitation

In the above consideration, we have assumed the spatial distribution of each atom ensemble is small, the excitation of the control atom is treated to be localized at a fixed position in the channel B, such that the interaction is described by the simple form of $V_{AB} = -C_6/d^6$. In reality, atoms in the ensemble spread in space [39]. For practical realization of the FIT and photon switch predicted here, the spatial dependence of the atom-atom interaction needs to be taken into account.

When there is a delocalization of the control-atom excitation over the channel B, the inter-channel interaction takes the form $V_{AB} = -C_6/|\mathbf{d} + \mathbf{r}_B|^6$. Here $d = |\mathbf{d}|$ is the center-of-mass (COM) separation between the channels A and B, and $r_B = |\mathbf{r}_B|$ is the distance of the control excitation relative to the COM of the channel B; see Fig. 6(a). Under such a consideration, we can obtain $\mathbf{r}_B$-dependent ρ_{21}^A, which reads

$$\rho_{21}^A(\mathbf{r}_B) \simeq -\frac{2V_{AB}(\mathbf{r}_B)\rho_{31,33}^{AB}(\mathbf{r}_B)}{\Omega}. \qquad (13)$$
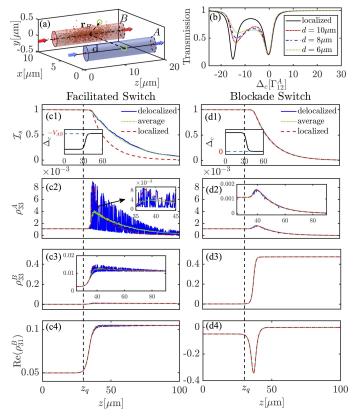
FIG. 6. **FIT with delocalized control-atom excitation**. (a) Schematic of the delocalized control-atom excitation in the channel B. The delocalization modifies the atom-atom interaction form from $V_{AB} = -C_6/d^6$ to $V_{AB} = -C_6/|\mathbf{d} + \mathbf{r}_B|^6$, here $d = |\mathbf{d}|$ is the center-of-mass separation between the A and B channels and $r_B = |\mathbf{r}_B|$ is the relative variation of the control excitation. (b) Photon transmission T as a function of Δ_c for different d, but with fixed $V_{AB}(r_B = 0) = 15\Gamma_{12}^A$, when the photon propagates to distance $L = 20\mu m$. Solid black line: the result of the ideal FIT (i.e. the case for localized control-atom excitation). (c) is similar to Fig. 5(b). To launch facilitated (blockade) switch, here Δ_c is changed from the far-detuned value to $-V_{AB}$ (or 0). (c1)-(c3) show the relative intensity of the probe field I_s and the Rydberg population $\rho_{33}^{A(B)}$ in the facilitated regime; (d1)-(d3) are similar to (c1)-(c3) but for the blockade regime. Blue curves in these figures are results of single trajectory simulation in the delocalization regime. Their mean values are calculated by casting 300 trajectories for different initial delocalized distribution (see green-dotted line). The coherence of the control atom is modified during the operation of the photon switch, manifested by the real $\text{Re}(\rho_{31}^B)$ of the atomic coherence [see panel (c4) and (d4)]. System parameters used in the simulation are $\Omega = \Omega_c = 3\Gamma_{12}^A$ and $\mathcal{N}_A = 3 \times 10^{12}\text{cm}^{-3}$.

Then optical susceptibility of the probe field is given by

$$\chi_p = \int d\mathbf{r}_B f(\mathbf{r}_B) \frac{\hbar\varepsilon_0}{\mathcal{N}_A \mu_{21}^2 \Omega_p} \rho_{21}^A(\mathbf{r}_B), \qquad (14)$$

where $f(\mathbf{r}_B)$ is a normalized distribution function describing the spatial delocalization of the control-atom excitation in the channel B. For simplicity, we assume $f(\mathbf{r}_B)$ takes the form of the Gaussian distribution, i.e. $f(\mathbf{r}_B) = 1/(\sqrt{\pi}\sigma)\exp[-(\mathbf{r}_B/\sigma)^2])$, with σ being the distribution width. The delocalization degree can be characterized by using parameter $\max(r_B)/d$.

Fig. 6(a) shows the schematic of the delocalized control-atom excitation in the channel B with a three-dimensional Gaussian-shaped distribution. To get a quantitative result of the behavior of single-photon switch in the presence of the delocalized control-atom excitation, a numerical simulation is carried out by using a combination of the four-order Runge-Kutta and finite difference methods to solve the corresponding coupled Maxwell-Bloch equations. In the simulation, we average the transmission T over different sites until the result converges.

Shown in Fig. 6(b) is the transmission T as a function of Δ_c for different separation d, but with $V_{AB}(r_B = 0) = 15\Gamma_{12}^A$. To obtain such an interaction strength, it requires $C_6 = 2.68 \times 10^4 \text{GHz} \cdot \mu m^6$ (with state $|93S\rangle$) for $d = 6\mu m$ and $C_6 = 5.77 \times 10^5 \text{GHz} \cdot \mu m^6$ (with state $|122S\rangle$) for $d = 10\mu m$ in Rb atom. We can see that, in the presence of the delocalized control-atom excitation, the FIT can still be observed. However, in comparison with the case of the localization regime (i.e., the regime with no position fluctuation of the control-atom excitation), there has a slight shift on the absorption peak located at $\Delta_c = -V_{AB}$ (shown by the black solid line). In addition, in the delocalization regime, an inhomogeneous broadening for the FIT peak occurs; as d decreases, the delocalization degree of the control-atom excitation increases, and the FIT peak becomes smaller. Consequently, to realize a robust FIT, the system must have strong Rydberg interactions, larger separation between the two channels, and tightly-focused control field.

To test the protocol of single-photon switch, we have conducted a simulation similar to that shown in Fig. 5(b), but with delocalized control-atom excitation here. Fig. 6(c1) shows the results of the relative probe-field intensity $\mathcal{I}_s$ as a function of z, for regimes of the delocalization (blue solid line) and localization (red dashed line) are given. We see that $\mathcal{I}_s$ decreases slower in the delocalization regime but still approaches to zero within a short propagation distance. Drawn in Fig. 6(c2) [Fig. 6(c3)] is the behavior of the Rydberg population ρ_{33}^A (ρ_{33}^B). One sees that, due to the delocalized excitation, both ρ_{33}^A and ρ_{33}^B exhibit large fluctuations; however, their envelopes are still facilitated, and captured well with the corresponding localized curves, respectively. To see the average behaviors of $\mathcal{I}_s$ and $\rho_{33}^{A(B)}$ in the presence of the fluctuations, in the simulation 300 trajectories for different initial delocalization distributions are considered, and these quantities are evaluated by calculating their mean values. The results of such an average are given by the green-dotted lines in the figure.

Shown in Fig. 6(d1)-(d3) are also for the quantities $\mathcal{I}_s$ and $\rho_{33}^{A(B)}$, but for the case of the blockade regime. Blue curves in these figures are results of single trajectory simulation in the delocalization regime. Their mean values are also calculated by casting 300 trajectories for different initial delocalized distributions (give by green-dotted lines). We see that the quality of the blockade switch is not to be significantly affected by the delocalized distribution of the control-atom excitation.

In order to know the coherence behavior of the Rydberg spin wave in the control channel B during the operation of the photon switch, we have calculated $\text{Re}(\rho_{31}^B)$ as a function of the propagation distance z, with the results being presented in

Fig. 6(c4) and Fig. 6(d4). We see that in the case of the facilitation regime Re(ρ_{31}^B) becomes increasingly protected during the operation of the switch [Fig. 6(c4)]; however, in the case of the blockade regime Re(ρ_{31}^B) first increases due to resonance driving, and then rapidly decays to zero [Fig. 6(d4)] as z increases. The reason for the protected coherence during the switch operation in the facilitation regime is due to the fact that the control atom is driven away from the resonance with the choice of $\Delta_c = -V_{AB}$. Thereby, the coherence of the control atom is not diminished even in the case of the photon scattering.

V. SUMMARY AND DISCUSSION

We have investigated the FIT effect in a dual-channel Rydberg atom setting. It is found that optical properties of the probe photon in the target channel can be actively controlled by varying laser detuning in the control channel. The FIT window emerges, and becomes wider and deeper as the interchannel Rydberg interaction increases. Using a dressed state approach, we have shown that the quantum interference pathways of the FIT are induced from the blockade and facilitated states. The FIT and its scaling on the interaction are examined both numerically and analytically. We have demonstrated that a contactless single-photon switch can be realized with FIT in the dual-channel system. Due to weak excitation under facilitated condition, coherence of the control channel is well protected during the operation of the switch. This work moreover opens new opportunities to directly detect Rydberg facilitation using the optical transmission of a neighboring atom ensemble.

Beyond the single-photon situation considered here, multiple Rydberg excitations can form strongly correlated states in spatially large atomic gases (e.g. Rydberg excitation crystals [72] and quantum scarring states [8]). An interesting question is whether one could use this contactless multi-channel setting to probe Rydberg excitations and phases through Rydberg interaction induced optical responses [73, 74]. This might provide new contactless detection methods without demolishing many-body coherence.

Appendix A: Multi-photon excitations in the control channel B

One can also adopt an two- and multi-photon excitation scheme in the control channel B. Here we gives a simple description on a two-photon excitation scheme, shown in Fig. A1. In this scheme, the channel A is the same as that in
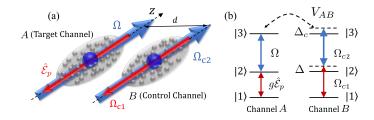

FIG. A1. **Two-photon excitation scheme for the control channel B**. (a) The channel A is the same as that of Fig. 1. The control channel B is however driven by a two-photon process, where the transition $|1\rangle \leftrightarrow |2\rangle$ ($|2\rangle \leftrightarrow |3\rangle$) is coupled by the control field of Rabi frequency Ω_{c1} (Ω_{c2}), with detuning Δ (Δ_c). (b) Level diagram of the system.

Fig. 1 in the main text, but the control channel B is a three-level system, where the first (second) control field with Rabi frequency Ω_{c1} (Ω_{c2}) drives the transition $|1\rangle \leftrightarrow |2\rangle$ ($|2\rangle \leftrightarrow |3\rangle$) with detuning Δ (Δ_c). Under rotating wave approximation, the two-atom Hamiltonian is given by $\hat{H} = \hat{H}_A + \hat{H}_B + \hat{H}_{int}$, with

$$\hat{H}_A = -\frac{\Omega_p}{2}\hat{\sigma}_{21}^A - \frac{\Omega}{2}\hat{\sigma}_{32}^A + \text{H.c.},$$

$$\hat{H}_B = -\left(\frac{\Omega_{c1}}{2}\hat{\sigma}_{21}^B + \frac{\Omega_{c2}}{2}\hat{\sigma}_{32}^B - \Delta\hat{\sigma}_{22}^B - \Delta_c\hat{\sigma}_{33}^B + \text{H.c.}\right),$$

$$\hat{H}_{int} = V_{AB}\hat{\sigma}_{33}^A\hat{\sigma}_{33}^B.$$

The dynamical behavior of such a system can be obtained by numerically solving the corresponding master equation. Shown in Fig. A2(a) is the result of Im(ρ_{21}^A) (the imaginary
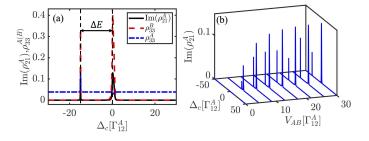

FIG. A2. **Atomic coherence and Rydberg excitations in the dual-channel model when the control channel B is driven by a two-photon process.** (a) FIT effect emerges in the absorption spectrum of the probe field, manifested by the imaginary part Im(ρ_{21}^A) of the atomic coherence ρ_{21}^A as a function of Δ_c (solid black line). Corresponding Rydberg excitations ρ_{33}^A (dot-dashed blue line) and ρ_{33}^B (dashed red line) are also plotted, where the channel A is blockaded at $\Delta_c = 0$, but facilitated around $\Delta_c = -V_{AB}$. (b) As V_{AB} increases, the FIT transparency window becomes wider and deeper. Two peaks are visible even for weak interaction strength (e.g, $V_{AB} = 5\Gamma_{12}^A$). System parameters used are $\Omega_{c1} = \Omega_p = 0.8\Gamma_{12}^A$, $\Omega_{c2} = \Omega = 4\Gamma_{12}^A$, and $\Delta = 10\Gamma_{12}^A$.

part of the atomic coherence ρ_{21}^A) as a function of Δ_c, plotted by the solid black line. The corresponding Rydberg excitations ρ_{33}^A and ρ_{33}^B are also illustrated by the dot-dashed blue

line and dashed red line, respectively. We see that the channel A is blockaded at $\Delta_c = 0$, but facilitated near $\Delta_c = -V_{AB}$. Consequently, the FIT phenomenon can emerge in such a system. i.e. two absorption peaks emerge in the profile of $\text{Im}(\rho_{21}^A)$ [Fig. A2(b)]. Moreover, the FIT transparency window becomes wider and deeper as V_{AB} increases. Notice that, due to the large single-photon detuning Δ in the channel B (which makes the effective Rabi frequency $\Omega_{\text{eff}} = \Omega_{c1}\Omega_{c2}/(2\Delta)$ small), the linewidth of the absorption peak (proportional to Ω_{eff}) is much narrower than that obtained by using the one-photon excitation of the channel B given in the main text. Thus by using such a scheme one can obtain a visible FIT doublet even for weak atomic interaction (e.g., $V_{AB} = 5\Gamma_{12}^A$). This result is also shown in Fig. 3(c) (the blue triangle line) in the main text, and agrees well with the dress-state theory described there.

Appendix B: Atomic coherences in stationary states

The Heisenberg equations for operators $\hat{\sigma}_{13}^A$ and $\hat{\sigma}_{12}^A$ read

$$i\left(\frac{\partial}{\partial t} + \gamma_{12}^A\right)\hat{\sigma}_{12}^A - \frac{\hat{\Omega}_p}{2}(\hat{\sigma}_{22}^A - \hat{\sigma}_{11}^A) + \frac{\Omega^*}{2}\hat{\sigma}_{13}^A = 0, \quad \text{(B1a)}$$

$$i\left(\frac{\partial}{\partial t} + \gamma_{13}^A\right)\hat{\sigma}_{13}^A - \frac{\hat{\Omega}_p}{2}\hat{\sigma}_{23}^A + \frac{\Omega}{2}\hat{\sigma}_{12}^A + V_{AB}\hat{\sigma}_{13}^A\hat{\sigma}_{33}^B = 0. \quad \text{(B1b)}$$

Taking the average (trace) on the above equations (i.e. $\rho_{ab}^{A(B)} \equiv \langle\sigma_{ba}^{A(B)}\rangle = \text{Tr}[\rho\sigma_{ba}^{A(B)}]$) and solving them for stationary states (i.e., $\partial/\partial t = 0$), we obtain the atomic coherence between the states $|1\rangle$ and $|2\rangle$:

$$\rho_{21}^A = \frac{-2V_{AB}\rho_{31,33}^{AB}\Omega^* + 2i(\rho_{11}^A - \rho_{22}^A)\gamma_{13}^A\Omega_p + \rho_{32}^A\Omega^*\Omega_p}{\Omega^2 + 4\gamma_{12}^A\gamma_{13}^A}. \quad \text{(B2)}$$

where $\rho_{31,33}^{AB} \equiv \langle\hat{\sigma}_{13}^A\hat{\sigma}_{33}^B\rangle$ is two-body DM element (or called two-body correlator). The terms related to the damping rate γ_{13}^A are very small (e.g., 100μs) and hence can be neglected. Moreover, since the probe field in the channel A is weak, ρ_{32}^A is negligible. Under these considerations, ρ_{21}^A can be reduced to

$$\rho_{21}^A \simeq -\frac{2V_{AB}\rho_{31,33}^{AB}}{\Omega}. \quad \text{(B3)}$$

We see that ρ_{21}^A depends mainly on the two-body density matrix element $\rho_{31,33}^{AB}$. From the result illustrated in Fig. 2(d) of the main text, one can see that Eq. (B3) can capture well with that obtained by solving the master equation numerically.

To get ρ_{21}^A, one must solve the equations of motion for two-body correlators $\rho_{ab,cd}^{AB}$ ($a, b, c, d = 1, 2, 3$). For saving space, we do not list these equation here. For more detail, see [75].

Appendix C: Dressed-state picture for the FIT

As shown in Fig. 3(a) in the main text, the interaction-dressed subspace is considered with the basis $\{|2_A\rangle, |3_A\rangle, |1_B\rangle, |3_B\rangle\}$. The Hamiltonian of this subspace reads

$$H_0 = \begin{bmatrix} 0 & -\Omega_c^*/2 & -\Omega^*/2 & 0 \\ -\Omega_c/2 & \Delta_c & 0 & -\Omega^*/2 \\ -\Omega/2 & 0 & 0 & -\Omega_c^*/2 \\ 0 & -\Omega/2 & -\Omega_c/2 & \Delta_c + V_{AB} \end{bmatrix}.$$

After neglecting the small damping (i.e. spontaneous emission and dephasing) in the system, the eigenvalue (eigenstate) ϵ_j ($|\psi_j\rangle$) of the subspace can be obtained by diagonalizing the above Hamiltonian, with the result sketched in Fig. 3(b) of the main text.

In particular, for the zero eigenvalue ($\epsilon_j = 0$), the probe field Ω_p can resonantly drive the transition from $|1_A\rangle$ to dressed subspace at the detuning defined by

$$\Delta_c^\pm = -\frac{V_{AB}}{2} \pm \frac{\sqrt{V_{AB}^2 + [(\Omega^2 - \Omega_c^2)/\Omega]^2}}{2}. \quad \text{(C1)}$$

In the strong interaction regime (i.e. $V_{AB} \gg \Omega, \Omega_c$), we have $\Delta_c^+ \simeq 0$ and $\Delta_c^- \simeq -V_{AB}$. By adiabatically sweeping Δ_c, the system can respectively excited to the Rydberg blockade and facilitation states, with the eigen state functions given by

$$|\Psi_E\rangle = \frac{1}{\sqrt{2}}(|3_A 1_B\rangle - |2_A 3_B\rangle), \quad \text{for } \Delta_c = \Delta_c^+, \quad \text{(C2a)}$$

$$|\Psi_F\rangle = \frac{1}{\sqrt{2}}(|3_A 3_B\rangle - |2_A 1_B\rangle), \quad \text{for } \Delta_c = \Delta_c^-. \quad \text{(C2b)}$$

However, due to the large decay of the level $|2_A\rangle$ (which is not included in the calculation on the eigenstates), entangled state $|\Psi_E\rangle$ rapidly evolves to trivial blockade state $|\Psi_B\rangle = |1_A 3_B\rangle$. The energy gap between $|\Psi_E\rangle$ and $|\Psi_B\rangle$ is

$$\Delta E = \sqrt{V_{AB}^2 + (\Omega - \Omega_c^2/\Omega)^2} \simeq V_{AB}, \quad \text{(C3)}$$

which is plotted (with dashed red line) in Fig. 3(c) of the main text. We find that the result of this dressed-state approach can capture the numerical data very well in the interaction dominant regime.

Appendix D: FIT in the three-atom model

To explore the influence of the target-target (TT) interaction (described by V_{TT}) in systems with multi-channels, here we consider a simple three-atom scenario with one control channel and two target channels; see the inset of Fig. A3(a1) and the corresponding caption. For simplicity, we assume that the control-target (CT) interaction V_{CT} is fixed, but V_{TT} can be changed by varying position of target channels on the shell.

The FIT behavior in such a system is investigated by solving the corresponding Maxwell-Bloch equations of the model, with results given by in Fig. A3. Panel (a1) shows the FIT spectrum $\text{Im}(\rho_{21})$ for the target-channel as a function of Δ_c and V_{TT}, with $V_{CT} = 15\Gamma_{12}^A$. We see that it exhibits two peaks even V_{TT} is strong. Illustrated in panel (a2) is the contour map of V_{TT} as a function of Δ_c, sketched with $\text{Im}[\rho_{21} - \rho_{12}(V_{TT} = 0)]$. One sees that it reaches a saturation as V_{TT} increases. For
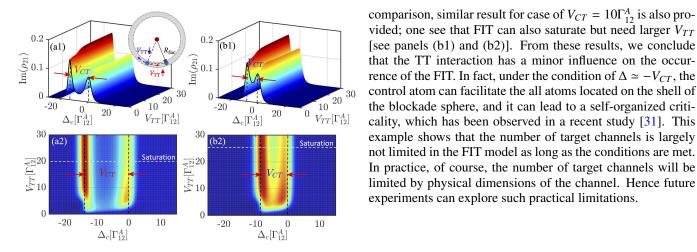
FIG. A3. **Three-atom model**. (a1) FIT spectrum $\text{Im}(\rho_{21})$ for the target channel as functions of Δ_c and V_{TT}, which exhibits double peaks even for a strong V_{TT}, with $V_{CT} = 15\Gamma_{12}^A$. The inset shows the geometry of the system, in which the control channel (red circle) locates at the center of a ring (with radius R_{fac}), and the target channels (two blue circles) locate on the shell. (a2) The corresponding contour map as functions of Δ_c and V_{TT} is sketched with $\text{Im}[\rho_{21} - \rho_{12}(V_{TT} = 0)]$. It is clear to see that the results reach saturation as V_{TT} increases. (b1) and (b2) are similar to (a1) and (a2) but with $V_{CT} = 10\Gamma_{12}^A$.

comparison, similar result for case of $V_{CT} = 10\Gamma_{12}^A$ is also provided; one see that FIT can also saturate but need larger V_{TT} [see panels (b1) and (b2)]. From these results, we conclude that the TT interaction has a minor influence on the occurrence of the FIT. In fact, under the condition of $\Delta \simeq -V_{CT}$, the control atom can facilitate the all atoms located on the shell of the blockade sphere, and it can lead to a self-organized criticality, which has been observed in a recent study [31]. This example shows that the number of target channels is largely not limited in the FIT model as long as the conditions are met. In practice, of course, the number of target channels will be limited by physical dimensions of the channel. Hence future experiments can explore such practical limitations.

[1] M. Saffman, T. G. Walker, and K. Mølmer, Rev. Mod. Phys. **82**, 2313 (2010).

[2] C. Murray and T. Pohl, Advances In Atomic, Molecular, and Optical Physics, Vol. 65 (Academic Press, 2016) pp. 321 – 372.

[3] C. S. Adams, J. D. Pritchard, and J. P. Shaffer, J. Phys. B **53**, 012002 (2019).

[4] A. Browaeys and T. Lahaye, Nat. Phys. **16**, 132 (2020).

[5] T. E. Lee, H. Häffner, and M. C. Cross, Phys. Rev. A **84**, 031402(R) (2011).

[6] H. Bernien, S. Schwartz, A. Keesling, H. Levine, A. Omran, H. Pichler, S. Choi, A. S. Zibrov, M. Endres, M. Greiner, V. Vuletić, and M. D. Lukin, Nature **551**, 579 (2017).

[7] I. Lesanovsky and H. Katsura, Phys. Rev. A **86**, 041601(R) (2012).

[8] C. J. Turner, A. A. Michailidis, D. A. Abanin, M. Serbyn, and Z. Papić, Nat. Phys. **14**, 745 (2018).

[9] D. Bluvstein, A. Omran, H. Levine, A. Keesling, G. Semeghini, S. Ebadi, T. T. Wang, A. A. Michailidis, N. Maskara, W. W. Ho, S. Choi, M. Serbyn, M. Greiner, V. Vuletić, and M. D. Lukin, Science **371**, 1355 (2021).

[10] S. Geier, N. Thaicharoen, C. Hainaut, T. Franz, A. Salzinger, A. Tebben, D. Grimshandl, G. Zürn, and M. Weidemüller, Science **374**, 1149 (2021).

[11] M. D. Lukin, M. Fleischhauer, R. Cote, L. M. Duan, D. Jaksch, J. I. Cirac, and P. Zoller, Phys. Rev. Lett. **87**, 037901 (2001).

[12] N. L. R. Spong, Y. Jiao, O. D. W. Hughes, K. J. Weatherill, I. Lesanovsky, and C. S. Adams, Phys. Rev. Lett. **127**, 063604 (2021).

[13] A. W. Carr and M. Saffman, Phys. Rev. Lett. **111**, 033607 (2013).

[14] Y. Jau, A. Hankin, T. Keating, I. H. Deutsch, and G. W. Biedermann, Nat. Phys. **12**, 71–74 (2016).

[15] M. Khazali, K. Heshami, and C. Simon, Phys. Rev. A **91**, 030301(R) (2015).

[16] Y. Liu, Y. Sun, Z. Fu, P. Xu, X. Wang, X. He, J. Wang, and M. Zhan, Phys. Rev. Applied **15**, 054020 (2021).

[17] Y. Liu, L. Li, and Y. Ma, Phys. Rev. Research **4**, 013008 (2022).

[18] J. A. Sedlacek, A. Schwettmann, H. Kübler, R. Löw, T. Pfau, and J. P. Shaffer, Nat. Phys. **8**, 819 (2012).

[19] M. Jing, Y. Hu, J. Ma, H. Zhang, L. Zhang, L. Xiao, and S. Jia, Nat. Phys. **16**, 911 (2020).

[20] D. V. Vasilyev, A. Grankin, M. A. Baranov, L. M. Sieberer, and P. Zoller, PRX Quantum **1**, 020302 (2020).

[21] S.-L. Su, F.-Q. Guo, J.-L. Wu, Z. Jin, X. Q. Shao, and S. Zhang, Europhys. Lett. **131**, 53001 (2020).

[22] W. Li, D. Viscor, S. Hofferberth, and I. Lesanovsky, Phys. Rev. Lett. **112**, 243601 (2014).

[23] C. Ates, T. Pohl, T. Pattard, and J. M. Rost, Phys. Rev. Lett. **98**, 023002 (2007).

[24] N. Malossi, M. M. Valado, S. Scotto, P. Huillery, P. Pillet, D. Ciampini, E. Arimondo, and O. Morsch, Phys. Rev. Lett. **113**, 023006 (2014).

[25] H. Schempp, G. Günter, M. Robert-de Saint-Vincent, C. S. Hofmann, D. Breyel, A. Komnik, D. W. Schönleber, M. Gärttner, J. Evers, S. Whitlock, and M. Weidemüller, Phys. Rev. Lett. **112**, 013002 (2014).

[26] M. Marcuzzi, J. c. v. Minář, D. Barredo, S. de Léséleuc, H. Labuhn, T. Lahaye, A. Browaeys, E. Levi, and I. Lesanovsky, Phys. Rev. Lett. **118**, 063606 (2017).

[27] F. Liu, Z.-C. Yang, P. Bienias, T. Iadecola, and A. V. Gorshkov, Phys. Rev. Lett. **128**, 013603 (2022).

[28] I. Lesanovsky and J. P. Garrahan, Phys. Rev. A **90**, 011603(R) (2014).

[29] C. Pérez-Espigares, M. Marcuzzi, R. Gutiérrez, and I. Lesanovsky, Phys. Rev. Lett. **119**, 140401 (2017).

[30] T. Wintermantel, M. Buchhold, S. Shevate, M. Morgado,

Y. Wang, G. Lochead, S. Diehl, and S. Whitlock, Nat. Commun. **12**, 103 (2021).

[31] S. Helmrich, A. Arias, G. Lochead, T. M. Wintermantel, M. Buchhold, S. Diehl, and S. Whitlock, Nature **577**, 481 (2020).

[32] D.-S. Ding, H. Busche, B.-S. Shi, G.-C. Guo, and C. S. Adams, Phys. Rev. X **10**, 021023 (2020).

[33] T. Amthor, C. Giese, C. S. Hofmann, and M. Weidemüller, Phys. Rev. Lett. **104**, 013001 (2010).

[34] R. Gutiérrez, C. Simonelli, M. Archimi, F. Castellucci, E. Arimondo, D. Ciampini, M. Marcuzzi, I. Lesanovsky, and O. Morsch, Phys. Rev. A **96**, 041602(R) (2017).

[35] S. Bai, X. Tian, X. Han, Y. Jiao, J. Wu, J. Zhao, and S. Jia, New J. Phys. **22**, 013004 (2020).

[36] A. K. Mohapatra, T. R. Jackson, and C. S. Adams, Phys. Rev. Lett. **98**, 113003 (2007).

[37] B. He, A. V. Sharypov, J. Sheng, C. Simon, and M. Xiao, Phys. Rev. Lett. **112**, 133606 (2014).

[38] D. Viscor, W. Li, and I. Lesanovsky, New J. Phys. **17**, 033007 (2015).

[39] H. Busche, P. Huillery, S. W. Ball, T. Ilieva, M. P. A. Jones, and C. S. Adams, Nat. Phys. **13**, 655–658 (2017).

[40] J. D. Thompson, T. L. Nicholson, Q.-Y. Liang, S. H. Cantu, A. V. Venkatramani, S. Choi, I. A. Fedorov, D. Viscor, T. Pohl, M. D. Lukin, and V. Vuletić, Nature **542**, 206 (2017).

[41] M. Khazali, C. R. Murray, and T. Pohl, Phys. Rev. Lett. **123**, 113605 (2019).

[42] C. Chen, F. Yang, X. Wu, C. Shen, M. K. Tey, and L. You, Phys. Rev. A **103**, 053303 (2021).

[43] J. D. Pritchard, D. Maxwell, A. Gauguet, K. J. Weatherill, M. P. A. Jones, and C. S. Adams, Phys. Rev. Lett. **105**, 193603 (2010).

[44] J. Hwang, M. Pototschnig, R. Lettow, G. Zumofen, A. Renn, S. Götzinger, and V. Sandoghdar, Nature **460**, 76 (2009).

[45] R. Bose, D. Sridharan, H. Kim, G. S. Solomon, and E. Waks, Phys. Rev. Lett. **108**, 227402 (2012).

[46] D. Englund, A. Majumdar, M. Bajcsy, A. Faraon, P. Petroff, and J. Vučković, Phys. Rev. Lett. **108**, 093604 (2012).

[47] V. Loo, C. Arnold, O. Gazzano, A. Lemaître, I. Sagnes, O. Krebs, P. Voisin, P. Senellart, and L. Lanco, Phys. Rev. Lett. **109**, 166806 (2012).

[48] T. Volz, A. Reinhard, M. Winger, A. Badolato, K. J. Hennessy, E. L. Hu, and A. Imamoğlu, Nature Photonics **6**, 605 (2012).

[49] M. Bajcsy, S. Hofferberth, V. Balic, T. Peyronel, M. Hafezi, A. S. Zibrov, V. Vuletic, and M. D. Lukin, Phys. Rev. Lett. **102**, 203902 (2009).

[50] D. O'Shea, C. Junge, J. Volz, and A. Rauschenbeutel, Phys. Rev. Lett. **111**, 193601 (2013).

[51] W. Chen, K. M. Beck, R. Bücker, M. Gullans, M. D. Lukin, H. Tanji-Suzuki, and V. Vuletić, Science **341**, 768 (2013).

[52] D. E. Chang, V. Vuletić, and M. D. Lukin, Nature Photonics **8**, 685 (2014).

[53] S. Baur, D. Tiarks, G. Rempe, and S. Dürr, Phys. Rev. Lett. **112**, 073901 (2014).

[54] H. Gorniaczyk, C. Tresp, J. Schmidt, H. Fedder, and S. Hofferberth, Phys. Rev. Lett. **113**, 053601 (2014).

[55] D. Tiarks, S. Baur, K. Schneider, S. Dürr, and G. Rempe, Phys. Rev. Lett. **113**, 053602 (2014).

[56] W. Li and I. Lesanovsky, Phys. Rev. A **92**, 043828 (2015).

[57] C. R. Murray, A. V. Gorshkov, and T. Pohl, New J. Phys. **18**, 092001 (2016).

[58] Y.-C. Yu, M.-X. Dong, Y.-H. Ye, G.-C. Guo, D.-S. Ding, and B.-S. Shi, Sci. China Phys. Mech. Astron. **63**, 110312 (2020).

[59] A. Derevianko, P. Kómár, T. Topcu, R. M. Kroeze, and M. D. Lukin, Phys. Rev. A **92**, 063419 (2015).

[60] V. Bendkowsky, B. Butscher, J. Nipper, J. P. Shaffer, R. Löw, and T. Pfau, Nature **458**, 1005 (2009).

[61] W. Li, T. Pohl, J. M. Rost, S. T. Rittenhouse, H. R. Sadeghpour, J. Nipper, B. Butscher, J. B. Balewski, V. Bendkowsky, R. Löw, and T. Pfau, Science **334**, 1110 (2011).

[62] F. Camargo, R. Schmidt, J. D. Whalen, R. Ding, G. Woehl, S. Yoshida, J. Burgdörfer, F. B. Dunning, H. R. Sadeghpour, E. Demler, and T. C. Killian, Phys. Rev. Lett. **120**, 083401 (2018).

[63] Z. Bai, C. S. Adams, G. Huang, and W. Li, Phys. Rev. Lett. **125**, 263605 (2020).

[64] D. A. Steck, "Alkali D Line Data," (2019).

[65] A. V. Gorshkov, A. André, M. D. Lukin, and A. S. Sørensen, Phys. Rev. A **76**, 033805 (2007).

[66] M. Fleischhauer and M. D. Lukin, Phys. Rev. A **65**, 022314 (2002).

[67] Q. Zhang and G. Huang, Phys. Rev. A **104**, 033714 (2021).

[68] H. Schempp, G. Günter, C. S. Hofmann, C. Giese, S. D. Saliba, B. D. DePaola, T. Amthor, M. Weidemüller, S. Sevinçli, and T. Pohl, Phys. Rev. Lett. **104**, 173602 (2010).

[69] M. Fleischhauer, A. Imamoglu, and J. P. Marangos, Rev. Mod. Phys. **77**, 633 (2005).

[70] M. M. Valado, C. Simonelli, M. D. Hoogerland, I. Lesanovsky, J. P. Garrahan, E. Arimondo, D. Ciampini, and O. Morsch, Phys. Rev. A **93**, 040701(R) (2016).

[71] C. Shou, Q. Zhang, W. Luo, and G. Huang, Opt. Express **29**, 9772 (2021).

[72] T. Pohl, E. Demler, and M. D. Lukin, Phys. Rev. Lett. **104**, 043002 (2010).

[73] B. Olmos, W. Li, S. Hofferberth, and I. Lesanovsky, Phys. Rev. A **84**, 041607(R) (2011).

[74] G. Günter, H. Schempp, M. Robert-de-Saint-Vincent, V. Gavryusev, S. Helmrich, C. S. Hofmann, S. Whitlock, and M. Weidemüller, Science **342**, 954 (2013).

[75] Z. Bai, W. Li, and G. Huang, Optica **6**, 309 (2019).